

# Highly Concentrated, Zwitterionic Ligand-Capped $Mn^{2+}$ : $CsPb(Br_xCl_{1-x})_3$ Nanocrystals as Bright Scintillators for Fast Neutron Imaging

Federico Montanarella, Kyle M. McCall,\* Kostiantyn Sakhatskyi, Sergii Yakunin, Pavel Trtik, Caterina Bernasconi, Ihor Cherniukh, David Mannes, Maryna I. Bodnarchuk, Markus Strobl, Bernhard Walfort, and Maksym V. Kovalenko\*



Cite This: *ACS Energy Lett.* 2021, 6, 4365–4373



Read Online

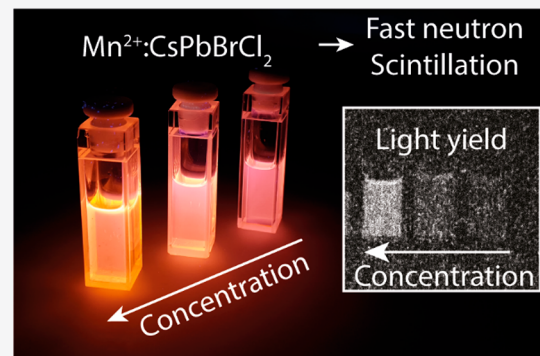
ACCESS |

Metrics & More

Article Recommendations

Supporting Information

**ABSTRACT:** Fast neutron imaging is a nondestructive technique for large-scale objects such as nuclear fuel rods. However, present detectors are based on conventional phosphors (typically microcrystalline ZnS:Cu) that have intrinsic drawbacks, including light scattering,  $\gamma$ -ray sensitivity, and afterglow. Fast neutron imaging with colloidal nanocrystals (NCs) was demonstrated to eliminate light scattering. While lead halide perovskite (LHP)  $FAPbBr_3$  NCs emitting brightly showed poor spatial resolution due to reabsorption, the  $Mn^{2+}$ -doped  $CsPb(BrCl)_3$  NCs with oleyl ligands had higher resolution because of large apparent Stokes shift but insufficient concentration for high light yield. In this work, we demonstrate a NC scintillator that features simultaneously high quantum yields, high concentrations, and a large apparent Stokes shift. In particular, we use long-chain zwitterionic ligand capping in the synthesis of  $Mn^{2+}$ -doped  $CsPb(BrCl)_3$  NCs that allows for attaining very high concentrations ( $>100$  mg/mL) of colloids. The emissive behavior of these ASC18-capped NCs was carefully controlled by compositional tuning that permitted us to select for high quantum yields (>50%) coinciding with Mn-dominated emission for minimal self-absorption. These tailored  $Mn^{2+}$ : $CsPb(BrCl)_3$  NCs demonstrated over 8 times brighter light yield than their oleyl-capped variants under fast neutron irradiation, which is competitive with that of near-unity  $FAPbBr_3$  NCs, while essentially eliminating self-absorption. Because of their rare combination of concentrations above 100 mg/mL and high quantum yields, along with minimal self-absorption for good spatial resolution,  $Mn^{2+}$ : $CsPb(BrCl)_3$  NCs have the potential to displace ZnS:Cu as the leading scintillator for fast neutron imaging.



Radiographic imaging with fast neutrons (>1 MeV) is increasingly sought as a nondestructive probe for large-scale objects that even high-energy X/ $\gamma$ -rays or thermal neutrons (~25 meV) cannot penetrate effectively.<sup>1–9</sup> This is because such high-energy neutrons offer low interaction cross sections for both high- and low-Z elements, whereas X/ $\gamma$ -rays are very sensitive to high-Z elements while thermal neutrons are especially interactive with low-Z elements such as Li or H.<sup>1</sup> However, fast neutron imaging is limited by the detector performance, where trade-offs are routinely made in efficiency, spatial resolution, and the decay time required between measurements.<sup>10–12</sup> Fast neutron detection for imaging relies on the elastic scattering of neutrons off nuclei, which then generates a recoil nucleus with small penetration depth; this recoil nucleus ionizes charge carriers and excites the scintillator.<sup>1,13–15</sup> Traditionally, the community has utilized

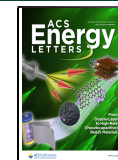
standard phosphors as the indirect detectors for recoil protons generated by scattering of fast neutrons.<sup>10,11,16</sup>

The leading material in the field is ZnS:Cu microparticles embedded in polypropylene (hereafter denoted ZnS:Cu(PP)) for high hydrogen density, which offers superior light yield<sup>10,11</sup> but suffers from scattering at the plastic–phosphor interface that limits spatial resolution with increasing thickness as well as deleterious minutes-long afterglow under fast neutron irradiation, greatly impacting the time needed to conduct the

Received: September 7, 2021

Accepted: November 8, 2021

Published: November 12, 2021



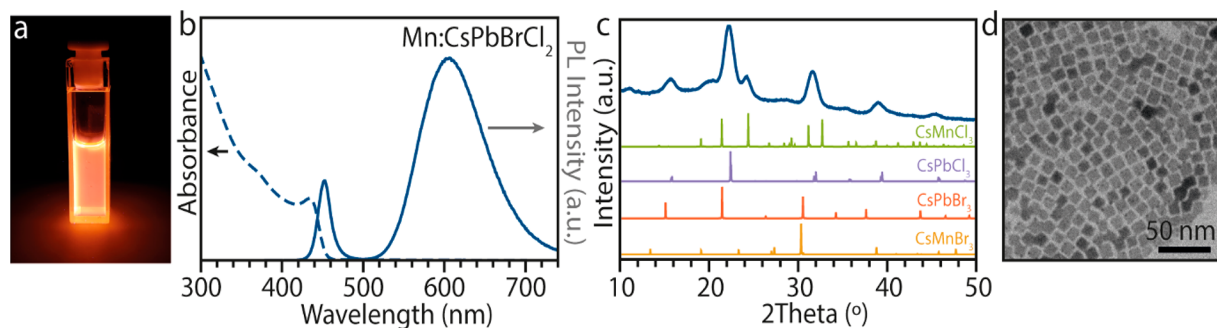


**Figure 1.** Optical and structural characterization of  $\text{Mn}^{2+}:\text{CsPb}(\text{BrCl})_3$  NCs. (a) Photograph of  $\text{Mn}^{2+}:\text{CsPb}(\text{BrCl})_3$  NCs solution under ultraviolet illumination. (b) Representative absorption (dashed line) and PL emission (solid line) spectrum of  $\text{Mn}^{2+}:\text{CsPb}(\text{BrCl})_3$  NCs. (c) Representative X-ray diffraction pattern of  $\text{Mn}^{2+}:\text{CsPb}(\text{BrCl})_3$  NCs (blue). XRD references correspond to  $\text{CsMnCl}_3$  (green, ICSD 2525),  $\text{CsPbCl}_3$  (purple, ICSD 243734),  $\text{CsPbBr}_3$  (red, ICSD 231017), and  $\text{CsMnBr}_3$  (orange, ICSD 2782). (d) Representative transmission electron micrograph of  $\text{Mn}^{2+}:\text{CsPb}(\text{BrCl})_3$  NCs. The average size is  $9.5 \pm 0.8$  nm.

repeated scans for computed tomography.<sup>10,11</sup> These intrinsic drawbacks of scattering and afterglow require a new approach for fast neutron imaging scintillators.

One particularly appealing class of phosphors are colloidal semiconducting nanocrystals (NCs), which naturally comprise a two-component, scattering-free system that includes emissive and hydrogen-dense components (NCs and solvent, respectively) in close contact. Among colloidal nanocrystals, lead halide perovskite (LHP) NCs have recently emerged as the new benchmark.<sup>17–19</sup> Their unmatched optical properties, on both the single-particle<sup>20,21</sup> and ensemble<sup>22–24</sup> levels, promoted them as powerful candidates for a variety of applications spanning from LEDs for displays<sup>25–28</sup> to fluorescent NCs for lighting.<sup>19,25</sup> We recently demonstrated the proof of concept by using colloidal NCs as recoil proton detectors, with these transparent solutions offering light yield without any evidence of scattering or afterglow.<sup>1</sup> We found that  $\text{FAPbBr}_3$  with a near-unity photoluminescence quantum yield (PL QY) was the brightest scintillator but that the spatial resolution suffered because of the low Stokes shift of many traditional NCs (e.g.,  $\text{FAPbBr}_3$ ), whereas the high-Stokes shift NCs exhibited low light yields either due to self-absorption or as a result of low concentration.<sup>1</sup> These results demonstrated that a successful fast neutron imaging scintillator requires a compelling and rare combination of high PL QY, high concentrations, and high Stokes shifts with low self-absorption; to the best of our knowledge, this combination is not possessed by any colloidal NC system to date.

With these design principles in mind, we turned to the ever-flexible LHP NCs as the ideal materials class to rationally design scintillating NCs. LHP NCs' flexible ionic structure, combined with relatively straightforward synthesis procedures, makes them ideal candidates for further functionalization via chemical manipulation. Major cation<sup>29–31</sup> and anion<sup>32,33</sup> exchange reactions have been widely explored as a powerful tool to control the final (optical) properties of LHP NCs, but also incorporation of elements, a process widely known as doping,<sup>34–36</sup> performed both *in situ*<sup>37–40</sup> or by postsynthetic treatment,<sup>41–44</sup> has been employed to functionalize, and chemically stabilize, LHP NCs for applications in the optical domain and beyond.<sup>45–50</sup>

While pure LHP NCs have bright emission, it is crucial to also achieve high concentrations and high Stokes shifts with suppressed optical reabsorption.<sup>51–53</sup> For LHP NCs, these optical characteristics are typically achieved via the doping of

$\text{CsPb}(\text{BrCl})_3$  nanocrystals with  $\text{Mn}^{2+}$  ions, in which optical reabsorption is minimized by decoupling the  $\text{Mn}^{2+}$  emission from the absorption of the perovskite matrix, resulting in an “apparent” large Stokes shift.<sup>42,54–62</sup> However, the relatively poor chemical stability and the intrinsically low concentration limit which can be achieved by using oleyl chains as ligands<sup>63</sup> hamper the efficiency of  $\text{Mn}^{2+}:\text{CsPb}(\text{BrCl})_3$  NCs as fast neutron scintillators.<sup>1</sup>

In this work, the development of a new synthesis yields  $\text{Mn}^{2+}$ -doped LHP NCs that pair excellent optical quality with drastically higher concentrations. This approach improves the light yield in this material system under fast neutron irradiation over 8 times that of the oleyl-capped  $\text{Mn}^{2+}$ -doped LHP NCs, permitting high light yields on par with the unity PL QY system  $\text{FAPbBr}_3$  without the detrimental self-absorption. These ASC18-capped  $\text{Mn}^{2+}:\text{CsPb}(\text{BrCl})_3$  NCs represent a substantial advance in this field, combining the beneficial properties of colloidal NCs (lack of scattering, no long-term afterglow) with both high light yield and good spatial resolution for fast neutron imaging.

Building upon the remarkable tunability of perovskite NCs, recent work in our group has demonstrated that enhanced stability and a broad range of concentrations can be achieved in undoped  $\text{CsPbX}_3$  ( $X = \text{Br}, \text{Cl}$ ) NCs through the appropriate choice of long-chain zwitterionic ligands.<sup>63,64</sup> Here, we adapted these syntheses to generate zwitterionic-capped- $\text{CsPb}(\text{BrCl})_3$  NCs doped with  $\text{Mn}^{2+}$  utilizing 3-(*N,N*-dimethyloctadecylammonio)propanesulfonate (ACSI8) as the ligand (see the Supporting Information for further details about the synthesis).<sup>64</sup> Their optical properties (Figure 1a) are similar to those observed for their oleyl-capped counterparts,<sup>1</sup> with a well-defined absorption edge (with clear excitonic features) and photoluminescence emission (PL) characterized by two contributions: one centered between 400 and 500 nm, associated with band-edge exciton recombination, and another centered between 580 and 650 nm corresponding to recombination from  $\text{Mn}^{2+}$  states. PL QY values of up to 60% can be achieved through appropriate compositional tuning. From a structural point of view, X-ray diffraction patterns (Figure 1b) are consistent with mixed  $\text{Br}^--\text{Cl}^-$  perovskite composition, and they show the occasional presence of  $\text{CsMnCl}_3$  impurities when high concentrations of  $\text{Mn}^{2+}$  precursor are used in the synthesis. Transmission electron microscopy (TEM) images (Figure 1d) reveal that the NCs are characterized by cubic shape with size of roughly  $\sim 10$  nm. The

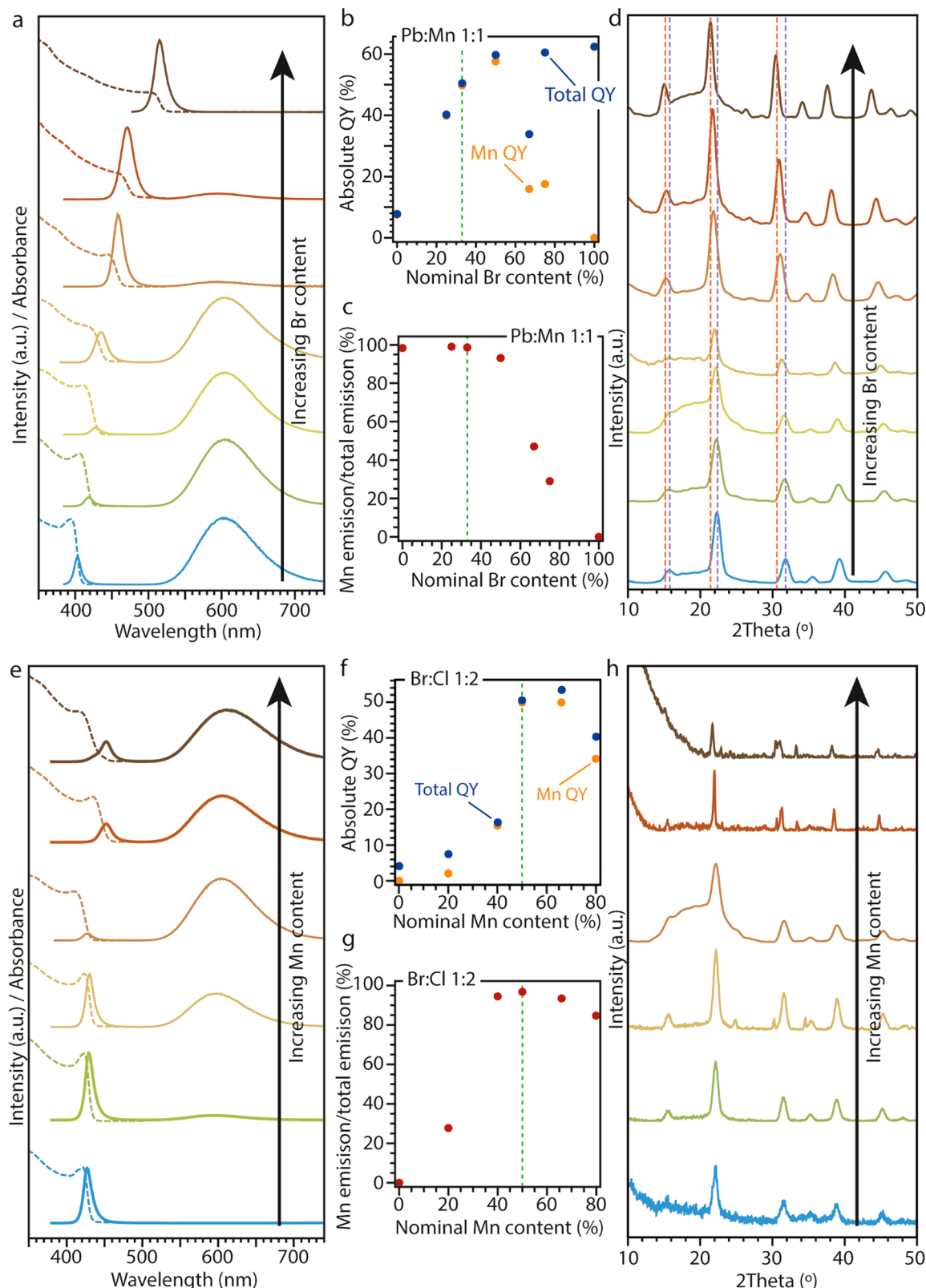


**Figure 2.** Tuning the optical properties of Mn<sup>2+</sup>:CsPb(BrCl)<sub>3</sub> NCs. (a) Absorption (dashed lines) and PL emission (solid lines) spectra of 50% Mn<sup>2+</sup>:CsPb(BrCl)<sub>3</sub> NCs with increasing Br<sup>-</sup> content (from bottom to top): 0, 25, 33, 50, 66, 75, and 100%. The nominal Mn<sup>2+</sup> content is constant at 50%. (b) Absolute QY of the total 50% Mn<sup>2+</sup>:CsPb(BrCl)<sub>3</sub> PL emission (blue dots) and of the Mn<sup>2+</sup> emission (orange dots) as a function of Br<sup>-</sup> content. The green dashed line marks the reference sample. (c) Percentage of the emission from Mn<sup>2+</sup> levels on the overall emission of the 50% Mn<sup>2+</sup>:CsPb(BrCl)<sub>3</sub> NCs as a function of Br<sup>-</sup> content. The green dashed line marks the reference sample. (d) XRD spectra of the 50% Mn<sup>2+</sup>:CsPb(BrCl)<sub>3</sub> samples of panels a–c. Br<sup>-</sup> content increases from bottom to top. The red dashed lines mark the positions of the main reflections of CsPbBr<sub>3</sub> (ICSD 231017), while the purple dashed lines mark the positions of the main reflections of CsPbCl<sub>3</sub> (ICSD 243734). (e) Absorption (dashed lines) and PL emission (solid lines) spectra of Mn<sup>2+</sup>:CsPbBrCl<sub>2</sub> NCs with increasing Mn content (from bottom to top): 0, 25, 33, 50, 66, 75, and 100%.

Figure 2. continued

nominal  $Mn^{2+}$  content (from bottom to top): 0, 20, 40, 50, 66, and 80%. The nominal  $Br^-$  content is constant at 33%. (f) Absolute QY of the total  $Mn^{2+}:CsPbBrCl_2$  PL emission (blue dots) and of the  $Mn^{2+}$  emission (orange dots) as a function of  $Mn^{2+}$  content. The green dashed line marks the reference sample. (g) Percentage of the emission from  $Mn^{2+}$  levels on the overall emission of the  $Mn^{2+}:CsPbBrCl_2$  NCs as a function of  $Mn^{2+}$  content. The green dashed line marks the reference sample. (h) XRD spectra of the  $Mn^{2+}:CsPbCl_2$  samples of panels e–g.  $Mn^{2+}$  content increases from bottom to top.

presence of zwitterionic capping ligands on the surface of the NCs greatly enhances the chemical stability and enables significantly higher concentrations of NCs in solution compared to their counterparts stabilized by oleates. Typically, with ASC18 as stabilizing agent, concentrations of  $\sim 100$  mg/mL were achieved (Table S1), in agreement with previous reports;<sup>64</sup> this is an increase of 2 orders of magnitude compared to the oleyl-stabilized NCs from the previous study.<sup>1</sup> We also attempted to utilize lecithin as the capping ligand to obtain even higher concentrations as reported for undoped NCs,<sup>63</sup> but while we achieved concentrations of  $\sim 400$  mg/mL (Figure S1), the PL QY of these NCs never exceeded 10%; this evidence implies that the ligand shell also plays a pivotal role in determining the final optical properties of the NCs.

We then sought to leverage the tunability of these doped perovskite NCs to achieve the high (apparent) Stokes shift and PL QYs required for efficient fast neutron scintillation. The optical properties of the NCs can be widely tuned by varying the ratios between the halide precursors during the synthesis. When increasing the  $Br^-$  content at the expense of the  $Cl^-$  content while keeping the  $Mn^{2+}$  content constant (nominal 50%), we observe that the absorption band edge and the band-edge PL emission shift toward longer wavelengths, while the  $Mn^{2+}$  PL shifts toward shorter wavelengths (Figure 2a–d), consistent with previous observations.<sup>55,65,66</sup> In particular, the PL emission (Figure 2a) associated with band-edge exciton recombination shifts from 403 nm for pure  $Mn^{2+}:CsPbCl_3$  to 515 nm for pure  $Mn^{2+}:CsPbBr_3$ , while the PL emission from  $Mn^{2+}$  states shifts from 604 to 595 nm; this latter effect has been attributed to a weakening of the crystal field induced by the expansion of the crystal lattice when  $Cl^-$  is substituted for  $Br^-$ .<sup>65</sup> At the same time, we also observe the disappearance of the excitonic feature in the absorption spectra of the NCs due to a relaxation of the quantum confinement, consistent with previous observations in anion exchange reactions.<sup>32,33</sup> Interestingly, the  $Br^-$  content strongly affects the ratio between the two components of the PL emission: the emission originating from the band-edge exciton recombination becomes dominant for a nominal  $Br^-$  content larger than 60%. This behavior is even more evident when considering the variation of the PL QY (Figure 2b) and of the amount of emission from the  $Mn^{2+}$  states (relative to the overall emission; Figure 2c). The overall PL QY scales with the  $Br^-$  content, increasing from a value of 9%, for pure  $Mn^{2+}:CsPbCl_3$ , to 62%, for nominal 50%  $Br^-$  content; for larger values of  $Br^-$  content, the overall PL QY remains constant. In contrast, the proportion (%) of the emission from  $Mn^{2+}$  states slightly increases, while being close to unity for increasing  $Br^-$  content, until it linearly decreases for  $Br^-$  content greater than 33%. This behavior can be understood when considering the competition between the two recombination processes (from band-edge states and  $Mn^{2+}$  states) and the exciton-to-activator ( $Mn^{2+}$ ) forward and backward energy transfer. As the  $Br^-$  content increases, the exciton radiative recombination rate decreases while the energy transfer rate increases, resulting in

an increase in the emission from  $Mn^{2+}$  states. At the same time, with increasing  $Br^-$  content, the energy difference between the band-edge and the  $Mn^{2+}$  states decreases, hence making the backward energy transfer more efficient. Furthermore, because the radiative recombination from band-edge states is much faster ( $\sim ns$ ) than the recombination from the  $Mn^{2+}$  states ( $\sim ms$ ),<sup>65</sup> this recombination process will be more favorable, effectively decreasing the proportion of excitons recombining from the  $Mn^{2+}$  states (for  $Br^-$  content greater than 33%).<sup>65</sup> From a structural point of view, the XRD patterns (Figure 2d) are consistent with the evolution from pure  $Mn^{2+}:CsPbCl_3$  perovskite NCs to pure  $Mn^{2+}:CsPbBr_3$  via mixed halide composition.

Beyond the traditional halide tuning that has helped popularize perovskite NCs, the addition of the  $Mn^{2+}$  dopant adds a further knob for controlling the resulting optical properties of  $Mn^{2+}:CsPb(BrCl)_3$  NCs by varying the ratio between  $Pb^{2+}$  and  $Mn^{2+}$  precursors during the synthesis. Keeping the  $Br^-$  content constant at 33% nominal (hereafter denoted  $Mn^{2+}:CsPbBrCl_2$ ) to maximize both the PL QY and the proportion of  $Mn^{2+}$  emission, we observe that the emission from  $Mn^{2+}$  states scales with the nominal  $Mn^{2+}$  content (Figure 2e–h). Furthermore, while the band edge emission remains constant at 427 nm, the  $Mn^{2+}$  emission shifts from 596 nm (for 20% nominal  $Mn^{2+}$  content) to 614 nm (for  $Mn^{2+}$  contents larger than 50%); this effect has previously been attributed to an increase of the crystal field.<sup>67–69</sup> Furthermore, we observe that for nominal  $Mn^{2+}$  content greater than 50%, both the absorption band edge and the band-edge emission are shifted toward longer wavelengths (absorption, from 423 to 436 nm; PL, from 427 to 452 nm); we attribute this shift to the larger size of the NCs in this doping regime, as we will show later. The increasingly dominant contribution of emission from  $Mn^{2+}$  states is clear when inspecting the dependence of the PL QY on the nominal  $Mn^{2+}$  content (Figure 2f,g). The PL QY steadily increases with increasing nominal  $Mn^{2+}$  content, from a value of 4%, for pure  $CsPbCl_2Br$ , to a maximum of 54%, for 66% nominal  $Mn^{2+}$  content; for higher  $Mn^{2+}$  contents a decrease in the PL QY is observed. Analogously, when considering the contribution of the  $Mn^{2+}$ -emission to the overall emission (Figure 2g), we observe that a maximum is reached for 50% nominal  $Mn^{2+}$  content, while for higher contents the values are lower. The peculiar optical behavior of  $Mn^{2+}:CsPbCl_2Br$  for nominal  $Mn^{2+}$  content greater than 50% can be understood by complementing the optical data with XRD structural data (Figure 2h). The XRD patterns for the nominal  $Mn^{2+}$  contents 0–50% are rather similar, highlighting the presence of mainly  $Mn^{2+}:CsPbCl_2Br$  with some minor impurities ascribable to the presence of  $CsMnCl_3$  and  $CsMnBr_3$  phases, which are the main byproducts of the synthesis. However, for samples with nominal  $Mn^{2+}$  content greater than 50%, the sharpness of the XRD reflections implies the average domain size to be much larger compared to the other samples. Inspection of electron micrographs of these samples (Figure S2 in the Supporting Information) show the

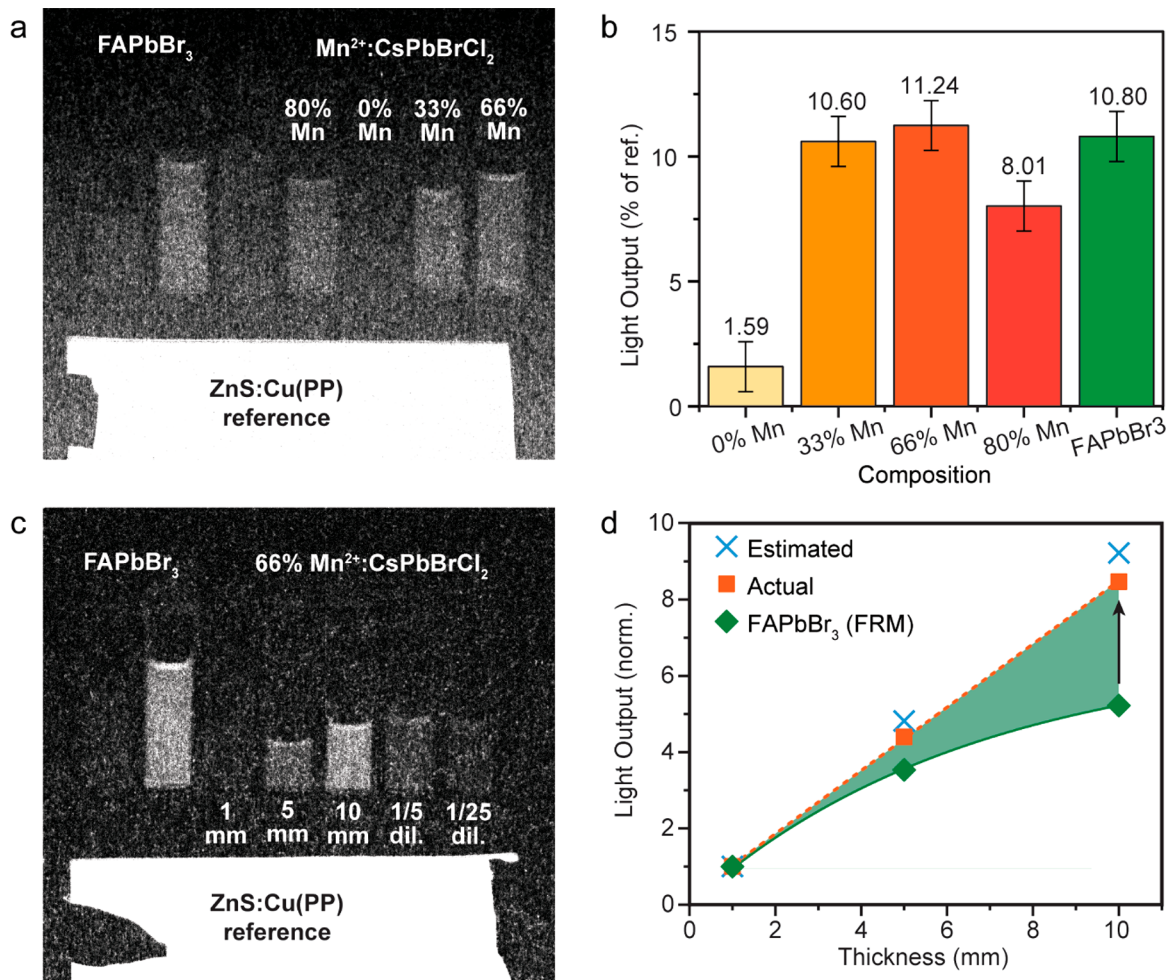


**Figure 3.** Fast neutron imaging with  $\text{Mn}^{2+}:\text{CsPbBrCl}_2$ . (a) Radiograph of  $\text{Mn}^{2+}:\text{CsPbBrCl}_2$  NC scintillators under fast neutron irradiation (average of 20 147.2 s exposures) as compared with  $\text{FAPbBr}_3$  nanocrystals<sup>1</sup> and a commercial  $\text{ZnS:Cu(PP)}$  screen, used here as a reference. (b) Light output of NC scintillators,<sup>1</sup> given as a percentage of the light yield obtained for the reference  $\text{ZnS:Cu(PP)}$  scintillator under identical conditions. (c) Fast neutron radiograph of 66%  $\text{Mn}^{2+}:\text{CsPbBrCl}_2$  thickness and concentration dependence (average of 10 147.2 s exposures). (d) Normalized light output vs sample thickness for 66%  $\text{Mn}^{2+}:\text{CsPbBrCl}_2$  NCs (cross symbols representing the expected relative light yield due to the fast neutron scattering of toluene at the given thickness) showing a nearly linear response, in sharp contrast to the  $\text{FAPbBr}_3$  NCs (previously measured at the FRM-II reactor beamline NECTAR) which suffer a sharp dropoff due to self-absorption (green fit line).<sup>1</sup> The dashed line is a guide to the eye.

presence of large cubic ( $\sim 50\text{--}100$  nm)  $\text{Mn}^{2+}:\text{CsPb}(\text{BrCl})_3$  NCs. A difference in reactivity between the  $\text{Mn}^{2+}$  and the  $\text{Pb}^{2+}$  precursors,  $\text{Mn}(\text{oleate})_2$  and  $\text{Pb}(\text{oleate})_2$ , respectively, is invoked as the origin of the much larger dimensions of the NCs synthesized in the presence of large quantities of  $\text{Mn}^{2+}$  precursor during the synthesis: the higher bond dissociation energy of the  $\text{Mn}-\text{O}$  bond (402 kJ/mol)<sup>70</sup> compared to the  $\text{Pb}-\text{O}$  bond (378 kJ/mol)<sup>70</sup> implies a lower reactivity of the  $\text{Mn}(\text{oleate})_2$  precursor, resulting therefore in larger NCs. This difference in reactivity can also explain the discrepancy between the nominal  $\text{Mn}^{2+}$  content introduced in the reaction vessel and the actual  $\text{Mn}^{2+}$  content incorporated in the NCs. Energy-dispersive X-ray analysis of the NCs with different nominal  $\text{Mn}^{2+}$  content emphasizes how only a marginal percentage of  $\text{Mn}^{2+}$  is incorporated in the NCs: for nominal 50%  $\text{Mn}^{2+}$  content, only 2.0 atom % is detected in the NCs, while for nominal 20%  $\text{Mn}^{2+}$  content, only 0.1 atom % is detected. We also remark that the exact position of the dopants (in the bulk or on the surface) was not determined, but further analysis, e.g., with EPR,<sup>34</sup> could discriminate between these

two cases. Nevertheless, these relatively small, incorporated amounts have a clear and important impact on the optical properties of the NCs.

Now that these tunable NCs have delivered high concentrations coinciding with excellent PL QYs and a large apparent Stokes shift, we explored the potential for these  $\text{Mn}^{2+}:\text{CsPb}(\text{BrCl})_3$  NCs as scintillators for fast neutron imaging. Given the importance of the Stokes shift in this application,<sup>1</sup> NC samples with the fixed Br/Cl ratio of 1:2 (where  $\text{Mn}^{2+}$ -emission dominates the emission spectrum, Figure 2e–h) with varying nominal  $\text{Mn}^{2+}$  content were compared, and the basic characteristics of these samples are detailed in Table S1. Fast neutron imaging measurements were conducted at the thermal neutron imaging beamline NEUTRA<sup>71</sup> of the SINQ spallation neutron source at the Paul Scherrer Institut. The thermal neutrons ( $\sim 25$  meV) were screened out of the beam by leaving the experimental shutter (composed of  $\text{B}_4\text{C}$  and Cd blocking layers) closed and adding a 2 mm Cd filter, leaving only the intermediate ( $>1$  eV) and fast neutrons ( $>1$  MeV) needed for the imaging experiments.

Samples were sealed in a light-tight box of the camera detector system that collected the incident light from the excited NC solutions, with a mirror ensuring that the camera is not in line with the beam to reduce background noise and camera irradiation.

A series of radiographs were measured for these  $\text{Mn}^{2+}:\text{CsPbBrCl}_2$  NCs under 147.2 s fast neutron exposure, with  $\text{FAPbBr}_3$  NCs and a commercial RC Tritec AG  $\text{ZnS}:\text{Cu(PP)}$  screen used for reference (Figure 3a). The background and asymmetry-corrected (Figure S3) light output are shown in Figure 3b as a percentage of that of the  $\text{ZnS}:\text{Cu(PP)}$  reference screen, and we observe that the scintillation intensity of these  $\text{Mn}^{2+}$ -containing NCs is comparable to the state-of-the-art  $\text{FAPbBr}_3$  NCs,<sup>1</sup> which have a quantum yield near unity. This validates the design principles described above, namely, that high Stokes shift and high concentration can overcome limitations of lower PL QY. The light output of these ASC18-capped  $\text{Mn}^{2+}:\text{CsPbBrCl}_2$  NCs is 8.65 times greater than that previously measured for oleyl-capped  $\text{Mn}^{2+}:\text{CsPbBrCl}_2$  NCs,<sup>1</sup> as determined using the relative light outputs of the  $\text{FAPbBr}_3$  reference NCs to account for the different beam characteristics (see the Supporting Information for details).<sup>1</sup> Notably, the undoped sample shows essentially no light output under the same conditions (likely due to the optical density of the highly concentrated colloid), further demonstrating the importance of high Stokes shift in achieving efficient scintillation in such dense samples. No afterglow was observed in 147.2 s images collected immediately after beam closure (Figure S4), though afterglow effects are reduced here because of the lower fast neutron flux of this beamline; therefore, this is not conclusive evidence against afterglow in these specific NCs. However, previous measurements for this system with oleyl ligands showed no afterglow, in stark contrast to  $\text{ZnS}:\text{Cu(PP)}$ .<sup>1</sup>

The brightest sample (nominally 66%  $\text{Mn}^{2+}$ ) was selected for further characterization of the thickness- and concentration-dependence of the fast neutron scintillation performance (Figure 3c). The concentration-dependent light output shows a continuous increase with increasing concentration (Figure S5a), indicating that the charge collection efficiency increases as we obtain more NCs per unit volume. Compared to prior efforts,<sup>1</sup> this increase is significantly closer to linearity, indicating that the self-absorption of these Stokes-shifted NCs is well below that of  $\text{FAPbBr}_3$  NCs and closer to self-trapped exciton systems such as the ionic liquid THTDPCl-PbCl<sub>2</sub> that recently demonstrated spatial resolution superior to that of the  $\text{ZnS}:\text{Cu}$  reference screens.<sup>72</sup>

Thickness-dependent measurements further confirm that the effect of self-absorption is substantially reduced in these doped NCs, as the light output is essentially linear and reaches 91.9% of the expected value (estimated using the stopping power of the solvent to 1 MeV neutrons) for a 10-fold increase in thickness (Figure 3d). Note that this expected value at 5 and 10 mm is overestimated as the beam includes both fast neutrons and intermediate neutrons, where the latter have smaller penetration depths and therefore would contribute to more light output at lower thicknesses; hence, the 91.9% value is a lower limit of the actual efficiency versus the expected values. This is a dramatic improvement over established NCs as  $\text{FAPbBr}_3$  and  $\text{CdSe}/\text{CdS}$  NCs suffered substantial self-absorption losses as the thickness increased, reaching only 56.7% and 37.0% of the expected value, respectively.<sup>1</sup> The scalability of the  $\text{Mn}^{2+}:\text{CsPbBrCl}_2$  system is thus vastly

superior to the prior NCs as both the concentration and thickness can be increased without reducing the signal, and the spatial resolution will similarly benefit as problematic reabsorption will not impact the sharpness of the measured radiographs.

In conclusion, a new synthesis based on zwitterionic ASC18 ligands yielded  $\text{Mn}^{2+}:\text{CsPb}(\text{BrCl})_3$  NCs which are colloidally stable to high concentrations of ~100 mg/mL while maintaining excellent optical quality. This synthesis extends the current technology of zwitterionic capped LHP NCs to doped systems, opening the doors to robust doped NCs in a wider concentration range. Furthermore, this system is immensely tunable through the halide and metal precursors, enabling us to rationally select the  $\text{Mn}^{2+}:\text{CsPbBrCl}_2$  system as having the ideal combination of high quantum yield (up to 53%) and dominant  $\text{Mn}^{2+}$  emission (97% of total emission). Fast neutron imaging experiments showed that these dense ASC18-capped NCs achieved light yields over 8 times greater than those of their oleyl-capped counterparts, matching that of near-unity  $\text{FAPbBr}_3$  NCs, despite being characterized by a quantum yield which was only half that. Furthermore, thickness and concentration-dependent measurements under fast neutron irradiation showcased the lack of self-absorption in this doped system, with essentially linear concentration dependence and drastically enhanced scalability with greater than 91.9% of the expected light yield achieved for a 10-fold increase in thickness. These results validate the design principles laid out by us previously, demonstrating that the designed  $\text{Mn}^{2+}:\text{CsPbBrCl}_2$  NCs offer an unparalleled combination of high concentrations (>100 mg/mL), quantum yields (>50%), and apparent Stokes shift (~1 eV) that permits efficient fast neutron scintillation without the problematic reabsorption that precludes  $\text{FAPbBr}_3$  NCs from achieving sufficient spatial resolution to displace  $\text{ZnS}:\text{Cu(PP)}$ . Future work will continue development of these NCs, including maximizing the concentration, utilizing solvents with higher hydrogen density than toluene, and preparing larger-scale detector screens.

## ASSOCIATED CONTENT

### Supporting Information

The Supporting Information is available free of charge at <https://pubs.acs.org/doi/10.1021/acsenergylett.1c01923>.

Nanocrystal synthesis, optical and structural characterization methods, and fast neutron imaging ([PDF](#))

## AUTHOR INFORMATION

### Corresponding Authors

Kyle M. McCall – *Laboratory of Inorganic Chemistry, Department of Chemistry and Applied Biosciences, ETH Zürich, CH-8093 Zürich, Switzerland; Laboratory for Thin Films and Photovoltaics, Empa – Swiss Federal Laboratories for Materials Science and Technology, CH-8600 Dübendorf, Switzerland; [orcid.org/0000-0001-8628-3811](#); Email: [Kyle.McCall@UTDallas.edu](mailto:Kyle.McCall@UTDallas.edu)*

Maksym V. Kovalenko – *Laboratory of Inorganic Chemistry, Department of Chemistry and Applied Biosciences, ETH Zürich, CH-8093 Zürich, Switzerland; Laboratory for Thin Films and Photovoltaics, Empa – Swiss Federal Laboratories for Materials Science and Technology, CH-8600 Dübendorf, Switzerland; [orcid.org/0000-0002-6396-8938](#); Email: [mvkovalenko@ethz.ch](mailto:mvkovalenko@ethz.ch)*

**Authors**

**Federico Montanarella** – Laboratory of Inorganic Chemistry, Department of Chemistry and Applied Biosciences, ETH Zürich, CH-8093 Zürich, Switzerland; Laboratory for Thin Films and Photovoltaics, Empa – Swiss Federal Laboratories for Materials Science and Technology, CH-8600 Dübendorf, Switzerland;  orcid.org/0000-0002-9057-7414

**Kostiantyn Sakhatskyi** – Laboratory of Inorganic Chemistry, Department of Chemistry and Applied Biosciences, ETH Zürich, CH-8093 Zürich, Switzerland; Laboratory for Thin Films and Photovoltaics, Empa – Swiss Federal Laboratories for Materials Science and Technology, CH-8600 Dübendorf, Switzerland

**Sergii Yakunin** – Laboratory of Inorganic Chemistry, Department of Chemistry and Applied Biosciences, ETH Zürich, CH-8093 Zürich, Switzerland; Laboratory for Thin Films and Photovoltaics, Empa – Swiss Federal Laboratories for Materials Science and Technology, CH-8600 Dübendorf, Switzerland;  orcid.org/0000-0002-6409-0565

**Pavel Trtik** – Laboratory for Neutron Scattering and Imaging, Paul Scherrer Institut, 5232 Villigen PSI, Switzerland

**Caterina Bernasconi** – Laboratory of Inorganic Chemistry, Department of Chemistry and Applied Biosciences, ETH Zürich, CH-8093 Zürich, Switzerland; Laboratory for Thin Films and Photovoltaics, Empa – Swiss Federal Laboratories for Materials Science and Technology, CH-8600 Dübendorf, Switzerland

**Ihor Cherniukh** – Laboratory of Inorganic Chemistry, Department of Chemistry and Applied Biosciences, ETH Zürich, CH-8093 Zürich, Switzerland; Laboratory for Thin Films and Photovoltaics, Empa – Swiss Federal Laboratories for Materials Science and Technology, CH-8600 Dübendorf, Switzerland

**David Mannes** – Laboratory for Neutron Scattering and Imaging, Paul Scherrer Institut, 5232 Villigen PSI, Switzerland

**Maryna I. Bodnarchuk** – Laboratory of Inorganic Chemistry, Department of Chemistry and Applied Biosciences, ETH Zürich, CH-8093 Zürich, Switzerland; Laboratory for Thin Films and Photovoltaics, Empa – Swiss Federal Laboratories for Materials Science and Technology, CH-8600 Dübendorf, Switzerland;  orcid.org/0000-0001-6597-3266

**Markus Strobl** – Laboratory for Neutron Scattering and Imaging, Paul Scherrer Institut, 5232 Villigen PSI, Switzerland

**Bernhard Walfort** – RC Tritec Ltd, 9053 Teufen, Switzerland

Complete contact information is available at:

<https://pubs.acs.org/10.1021/acsenergylett.1c01923>

**Notes**

The authors declare no competing financial interest.

**ACKNOWLEDGMENTS**

F.M. acknowledges support from ETH Zürich via the ETH Postdoctoral Fellowship (FEL-15 18-2) and from the Marie Skłodowska-Curie Actions COFUND Program. This work was financially supported by RC Tritec AG. and by ETH Zurich through the ETH+ Project SynMatLab: Laboratory for Multiscale Materials Synthesis. This work was partially supported by the European Union through Horizon 2020 (ERC Consolidator Grant SCALE-HALO, Grant Agreement No. [819740]) and by the Research and Innovation

Foundation of Cyprus, under the “New Strategic Infrastructure Units-Young Scientists” Program (Grant Agreement No. “Infrastructures/1216/0004”, Acronym “Nanosonics”). This work is based on experiments performed at the NEUTRA beamline of the Swiss spallation neutron source SINQ, Paul Scherrer Institut, Villigen, Switzerland.

**REFERENCES**

- (1) McCall, K. M.; Sakhatskyi, K.; Lehmann, E.; Walfort, B.; Losko, A. S.; Montanarella, F.; Bodnarchuk, M. I.; Krieg, F.; Kelestemur, Y.; Mannes, D.; Shynkarenko, Y.; Yakunin, S.; Kovalenko, M. V. Fast Neutron Imaging with Semiconductor Nanocrystal Scintillators. *ACS Nano* **2020**, *14* (11), 14686–14697.
- (2) Kardjilov, N.; Manke, I.; Hilger, A.; Strobl, M.; Banhart, J. Neutron Imaging in Materials Science. *Mater. Today* **2011**, *14* (6), 248–256.
- (3) Schillinger, B.; Beaudet, A.; Fedrigo, A.; Grazzi, F.; Kullmer, O.; Laaß, M.; Makowska, M.; Werneburg, I.; Zanolli, C. Neutron Imaging in Cultural Heritage Research at the FRM II Reactor of the Heinz Maier-Leibnitz Center. *J. Imaging* **2018**, *4* (1), 22.
- (4) Kardjilov, N.; Manke, I.; Woracek, R.; Hilger, A.; Banhart, J. Advances in Neutron Imaging. *Mater. Today* **2018**, *21* (6), 652–672.
- (5) Bücherl, T.; von Gostomski, C. L.; Baldauf, T. Fission Neutron Tomography of a 280-L Waste Package. *Materials Research Proceedings* **2018**, *15*, 299–304.
- (6) Bücherl, T.; Kalthoff, O.; von Gostomski, C. L. A Feasibility Study on Reactor Based Fission Neutron Radiography of 200-l Waste Packages. *Phys. Procedia* **2017**, *88* (September 2016), 64–72.
- (7) Börries, S.; Metz, O.; Pranzas, P. K.; Bellostas von Colbe, J. M.; Bücherl, T.; Dornheim, M.; Klassen, T.; Schreyer, A. Optimization and Comprehensive Characterization of Metal Hydride Based Hydrogen Storage Systems Using In-Situ Neutron Radiography. *J. Power Sources* **2016**, *328*, 567–577.
- (8) Mühlbauer, M. J.; Bücherl, T.; Kellermeier, M.; Knapp, M.; Makowska, M.; Schulz, M.; Zimnik, S.; Ehrenberg, H. Neutron Imaging with Fission and Thermal Neutrons at NECTAR at MLZ. *Phys. B* **2018**, *551* (August 2017), 359–363.
- (9) Nelson, R.; Vogel, S.; Hunter, J.; Watkins, E.; Losko, A.; Tremsin, A.; Borges, N.; Cutler, T.; Dickman, L.; Espy, M.; Gautier, D.; Madden, A.; Majewski, J.; Malone, M.; Mayo, D.; McClellan, K.; Montgomery, D.; Mosby, S.; Nelson, A.; Ramos, K.; Schirato, R.; Schroeder, K.; Sevanto, S.; Swift, A.; Vo, L.; Williamson, T.; Winch, N. Neutron Imaging at LANSCE—From Cold to Ultrafast. *J. Imaging* **2018**, *4* (2), 45.
- (10) Makowska, M.; Walfort, B.; Zeller, A.; Grünzweig, C.; Bücherl, T. Performance of the Commercial PP/ZnS:Cu and PP/ZnS:Ag Scintillation Screens for Fast Neutron Imaging. *J. Imaging* **2017**, *3* (4), 60.
- (11) Zboray, R.; Adams, R.; Morgano, M.; Kis, Z. Qualification and Development of Fast Neutron Imaging Scintillator Screens. *Nucl. Instrum. Methods Phys. Res., Sect. A* **2019**, *930* (December 2018), 142–150.
- (12) Zboray, R.; Adams, R.; Kis, Z. Scintillator Screen Development for Fast Neutron Radiography and Tomography and Its Application at the Beamline of the 10 MW BNC Research Reactor. *Appl. Radiat. Isot.* **2018**, *140* (April), 215–223.
- (13) Lehmann, E. H.; Vontobel, P.; Frei, G.; Brönnimann, C. Neutron Imaging—Detector Options and Practical Results. *Nucl. Instrum. Methods Phys. Res., Sect. A* **2004**, *531* (1–2), 228–237.
- (14) van Eijk, C. W. E. Inorganic Scintillators for Thermal Neutron Detection. *Radiat. Meas.* **2004**, *38* (4–6), 337–342.
- (15) Caruso, A. N. The Physics of Solid-State Neutron Detector Materials and Geometries. *J. Phys.: Condens. Matter* **2010**, *22* (44), 443201.
- (16) Bravar, U.; Bruillard, P. J.; Flckiger, E. O.; Macri, J. R.; McConnell, M. L.; Moser, M. R.; Ryan, J. M.; Woolf, R. S. Design and Testing of a Position-Sensitive Plastic Scintillator Detector for Fast Neutron Imaging. *IEEE Trans. Nucl. Sci.* **2006**, *53* (6), 3894–3903.

- (17) Akkerman, Q. A.; Rainò, G.; Kovalenko, M. V.; Manna, L. Genesis, Challenges and Opportunities for Colloidal Lead Halide Perovskite Nanocrystals. *Nat. Mater.* **2018**, *17* (5), 394–405.
- (18) Dey, A.; Ye, J.; De, A.; Debroye, E.; Ha, S. K.; Bladt, E.; Kshirsagar, A. S.; Wang, Z.; Yin, J.; Wang, Y.; Quan, L. N.; Yan, F.; Gao, M.; Li, X.; Shamsi, J.; Debnath, T.; Cao, M.; Scheel, M. A.; Kumar, S.; Steele, J. A.; Gerhard, M.; Chouhan, L.; Xu, K.; Wu, X.; Li, Y.; Zhang, Y.; Dutta, A.; Han, C.; Vincon, I.; Rogach, A. L.; Nag, A.; Samanta, A.; Korgel, B. A.; Shih, C.; Gamelin, D. R.; Son, D. H.; Zeng, H.; Zhong, H.; Sun, H.; Demir, H. V.; Scheblykin, I. G.; Morasero, I.; Stolarczyk, J. K.; Zhang, J. Z.; Feldmann, J.; Hofkens, J.; Luther, J. M.; Pérez-Prieto, J.; Li, L.; Manna, L.; Bodnarchuk, M. I.; Kovalenko, M. V.; Roeffaers, M. B. J.; Pradhan, N.; Mohammed, O. F.; Bakr, O. M.; Yang, P.; Müller-Buschbaum, P.; Kamat, P. V.; Bao, Q.; Zhang, Q.; Krahne, R.; Galian, R. E.; Stranks, S. D.; Bals, S.; Biju, V.; Tisdale, W. A.; Yan, Y.; Hoye, R. L. Z.; Polavarapu, L. State of the Art and Prospects for Halide Perovskite Nanocrystals. *ACS Nano* **2021**, *15* (7), 10775–10981.
- (19) Kovalenko, M. V.; Bodnarchuk, M. I. Lead Halide Perovskite Nanocrystals: From Discovery to Self-Assembly and Applications. *Chimia* **2017**, *71* (7–8), 461–470.
- (20) Becker, M. A.; Vaxenburg, R.; Nedelcu, G.; Sercel, P. C.; Shabaev, A.; Mehl, M. J.; Michopoulos, J. G.; Lambros, S. G.; Bernstein, N.; Lyons, J. L.; Stöferle, T.; Mahrt, R. F.; Kovalenko, M. V.; Norris, D. J.; Rainò, G.; Efros, A. L. Bright Triplet Excitons in Caesium Lead Halide Perovskites. *Nature* **2018**, *553* (7687), 189–193.
- (21) Rainò, G.; Nedelcu, G.; Protesescu, L.; Bodnarchuk, M. I.; Kovalenko, M. V.; Mahrt, R. F.; Stöferle, T. Single Cesium Lead Halide Perovskite Nanocrystals at Low Temperature: Fast Single-Photon Emission, Reduced Blinking, and Exciton Fine Structure. *ACS Nano* **2016**, *10* (2), 2485–2490.
- (22) Cherniukh, I.; Rainò, G.; Stöferle, T.; Burian, M.; Travasset, A.; Naumenko, D.; Amenitsch, H.; Erni, R.; Mahrt, R. F.; Bodnarchuk, M. I.; Kovalenko, M. V. Perovskite-Type Superlattices from Lead Halide Perovskite Nanocubes. *Nature* **2021**, *593* (7860), 535–542.
- (23) Rainò, G.; Becker, M. A.; Bodnarchuk, M. I.; Mahrt, R. F.; Kovalenko, M. V.; Stöferle, T. Superfluorescence from Lead Halide Perovskite Quantum Dot Superlattices. *Nature* **2018**, *563* (7733), 671–675.
- (24) Krieg, F.; Sercel, P. C.; Burian, M.; Andrusiv, H.; Bodnarchuk, M. I.; Stöferle, T.; Mahrt, R. F.; Naumenko, D.; Amenitsch, H.; Rainò, G.; Kovalenko, M. V. Monodisperse Long-Chain Sulfobetaine-Capped CsPbBr<sub>3</sub> Nanocrystals and Their Superfluorescent Assemblies. *ACS Cent. Sci.* **2021**, *7* (1), 135–144.
- (25) Kovalenko, M. V.; Protesescu, L.; Bodnarchuk, M. I. Properties and Potential Optoelectronic Applications of Lead Halide Perovskite Nanocrystals. *Science* **2017**, *358* (6364), 745–750.
- (26) Wang, H.-C.; Lin, S.-Y.; Tang, A.-C.; Singh, B. P.; Tong, H.-C.; Chen, C.-Y.; Lee, Y.-C.; Tsai, T.-L.; Liu, R.-S. Mesoporous Silica Particles Integrated with All-Inorganic CsPbBr<sub>3</sub> Perovskite Quantum-Dot Nanocomposites (MP-PQDs) with High Stability and Wide Color Gamut Used for Backlight Display. *Angew. Chem., Int. Ed.* **2016**, *55* (28), 7924–7929.
- (27) Liu, P.; Chen, W.; Wang, W.; Xu, B.; Wu, D.; Hao, J.; Cao, W.; Fang, F.; Li, Y.; Zeng, Y.; Pan, R.; Chen, S.; Cao, W.; Sun, X. W.; Wang, K. Halide-Rich Synthesized Cesium Lead Bromide Perovskite Nanocrystals for Light-Emitting Diodes with Improved Performance. *Chem. Mater.* **2017**, *29* (12), 5168–5173.
- (28) Yoon, H. C.; Kang, H.; Lee, S.; Oh, J. H.; Yang, H.; Do, Y. R. Study of Perovskite QD Down-Converted LEDs and Six-Color White LEDs for Future Displays with Excellent Color Performance. *ACS Appl. Mater. Interfaces* **2016**, *8* (28), 18189–18200.
- (29) van der Stam, W.; Geuchies, J. J.; Altantzis, T.; van den Bos, K. H. W.; Meeldijk, J. D.; Van Aert, S.; Bals, S.; Vanmaekelbergh, D.; de Mello Donegá, C. Highly Emissive Divalent Ion Doped Colloidal CsPb<sub>1</sub>–X<sub>x</sub>M<sub>x</sub>Br<sub>3</sub> Perovskite Nanocrystals through Cation Exchange. *J. Am. Chem. Soc.* **2017**, *139* (11), 4087–4097.
- (30) Nazarenko, O.; Kotyryba, M. R.; Yakunin, S.; Aebli, M.; Rainò, G.; Benin, B. M.; Wörle, M.; Kovalenko, M. V. Guanidinium-Formamidinium Lead Iodide: A Layered Perovskite-Related Compound with Red Luminescence at Room Temperature. *J. Am. Chem. Soc.* **2018**, *140* (11), 3850–3853.
- (31) Protesescu, L.; Yakunin, S.; Kumar, S.; Bär, J.; Bertolotti, F.; Masciocchi, N.; Guagliardi, A.; Grotevent, M.; Shorubalko, I.; Bodnarchuk, M. I.; Shih, C.-J.; Kovalenko, M. V. Dismantling the “Red Wall” of Colloidal Perovskites: Highly Luminescent Formamidinium and Formamidinium–Cesium Lead Iodide Nanocrystals. *ACS Nano* **2017**, *11* (3), 3119–3134.
- (32) Akkerman, Q. a; D’Innocenzo, V.; Accornero, S.; Scarpellini, A.; Petrozza, A.; Prato, M.; Manna, L. Tuning the Optical Properties of Cesium Lead Halide Perovskite Nanocrystals by Anion Exchange Reactions. *J. Am. Chem. Soc.* **2015**, *137* (32), 10276–10281.
- (33) Nedelcu, G.; Protesescu, L.; Yakunin, S.; Bodnarchuk, M. I.; Grotevent, M. J.; Kovalenko, M. V. Fast Anion-Exchange in Highly Luminescent Nanocrystals of Cesium Lead Halide Perovskites (CsPbX<sub>3</sub>, X = Cl, Br, I). *Nano Lett.* **2015**, *15* (8), 5635–5640.
- (34) Norris, D. J.; Efros, a. L.; Erwin, S. C. Doped Nanocrystals. *Science* **2008**, *319* (March), 1776–1779.
- (35) Pradhan, N.; Das Adhikari, S.; Nag, A.; Sarma, D. D. Luminescence, Plasmonic, and Magnetic Properties of Doped Semiconductor Nanocrystals. *Angew. Chem., Int. Ed.* **2017**, *56* (25), 7038–7054.
- (36) Mocatta, D.; Cohen, G.; Schattner, J.; Millo, O.; Rabani, E.; Banin, U. Heavily Doped Semiconductor Nanocrystal Quantum Dots. *Science* **2011**, *332* (2005), 77–81.
- (37) Parobek, D.; Dong, Y.; Qiao, T.; Son, D. H. Direct Hot-Injection Synthesis of Mn-Doped CsPbBr<sub>3</sub> Nanocrystals. *Chem. Mater.* **2018**, *30* (9), 2939–2944.
- (38) Begum, R.; Parida, M. R.; Abdelhady, A. L.; Murali, B.; Alyami, N. M.; Ahmed, G. H.; Hedhili, M. N.; Bakr, O. M.; Mohammed, O. F. Engineering Interfacial Charge Transfer in CsPbBr<sub>3</sub> Perovskite Nanocrystals by Heterovalent Doping. *J. Am. Chem. Soc.* **2017**, *139* (2), 731–737.
- (39) Yong, Z.-J.; Guo, S.-Q.; Ma, J.-P.; Zhang, J.-Y.; Li, Z.-Y.; Chen, Y.-M.; Zhang, B.-B.; Zhou, Y.; Shu, J.; Gu, J.-L.; Zheng, L.-R.; Bakr, O. M.; Sun, H.-T. Doping-Enhanced Short-Range Order of Perovskite Nanocrystals for Near-Unity Violet Luminescence Quantum Yield. *J. Am. Chem. Soc.* **2018**, *140* (31), 9942–9951.
- (40) Liu, M.; Zhong, G.; Yin, Y.; Miao, J.; Li, K.; Wang, C.; Xu, X.; Shen, C.; Meng, H. Aluminum-Doped Cesium Lead Bromide Perovskite Nanocrystals with Stable Blue Photoluminescence Used for Display Backlight. *Adv. Sci.* **2017**, *4* (11), 1700335.
- (41) Hills-Kimball, K.; Pérez, M. J.; Nagaoka, Y.; Cai, T.; Yang, H.; Davis, A. H.; Zheng, W.; Chen, O. Ligand Engineering for Mn<sup>2+</sup> Doping Control in CsPbCl<sub>3</sub> Perovskite Nanocrystals via a Quasi-Solid–Solid Cation Exchange Reaction. *Chem. Mater.* **2020**, *32* (6), 2489–2500.
- (42) Mir, W. J.; Mahor, Y.; Lohar, A.; Jagadeeswararao, M.; Das, S.; Mahamuni, S.; Nag, A. Postsynthesis Doping of Mn and Yb into CsPbX<sub>3</sub> (X = Cl, Br, or I) Perovskite Nanocrystals for Downconversion Emission. *Chem. Mater.* **2018**, *30* (22), 8170–8178.
- (43) Mondal, N.; De, A.; Samanta, A. Achieving Near-Unity Photoluminescence Efficiency for Blue-Violet-Emitting Perovskite Nanocrystals. *ACS Energy Lett.* **2019**, *4* (1), 32–39.
- (44) Das, S.; De, A.; Samanta, A. Ambient Condition Mg<sup>2+</sup> Doping Producing Highly Luminescent Green- and Violet-Emitting Perovskite Nanocrystals with Reduced Toxicity and Enhanced Stability. *J. Phys. Chem. Lett.* **2020**, *11* (3), 1178–1188.
- (45) Xu, L.; Yuan, S.; Zeng, H.; Song, J. A Comprehensive Review of Doping in Perovskite Nanocrystals/Quantum Dots: Evolution of Structure, Electronics, Optics, and Light-Emitting Diodes. *Mater. Today Nano* **2019**, *6*, 100036.
- (46) Milstein, T. J.; Kroupa, D. M.; Gamelin, D. R. Picosecond Quantum Cutting Generates Photoluminescence Quantum Yields over 100% in Ytterbium-Doped CsPbCl<sub>3</sub>Nanocrystals. *Nano Lett.* **2018**, *18* (6), 3792–3799.

- (47) Pan, G.; Bai, X.; Yang, D.; Chen, X.; Jing, P.; Qu, S.; Zhang, L.; Zhou, D.; Zhu, J.; Xu, W.; Dong, B.; Song, H. Doping Lanthanide into Perovskite Nanocrystals: Highly Improved and Expanded Optical Properties. *Nano Lett.* **2017**, *17* (12), 8005–8011.
- (48) Shapiro, A.; Heindl, M. W.; Horani, F.; Dahan, M.-H.; Tang, J.; Amouyal, Y.; Lifshitz, E. Significance of Ni Doping in  $\text{CsPbX}_3$  Nanocrystals via Postsynthesis Cation–Anion Coexchange. *J. Phys. Chem. C* **2019**, *123* (40), 24979–24987.
- (49) Akkerman, Q. A.; Meggiolaro, D.; Dang, Z.; De Angelis, F.; Manna, L. Fluorescent Alloy  $\text{CsPb}_{1-x}\text{Mn}_x\text{I}_3$  Perovskite Nanocrystals with High Structural and Optical Stability. *ACS Energy Lett.* **2017**, *2* (9), 2183–2186.
- (50) Zou, S.; Liu, Y.; Li, J.; Liu, C.; Feng, R.; Jiang, F.; Li, Y.; Song, J.; Zeng, H.; Hong, M.; Chen, X. Stabilizing Cesium Lead Halide Perovskite Lattice through Mn(II) Substitution for Air-Stable Light-Emitting Diodes. *J. Am. Chem. Soc.* **2017**, *139* (33), 11443–11450.
- (51) Coropceanu, I.; Bawendi, M. G. Core/Shell Quantum Dot Based Luminescent Solar Concentrators with Reduced Reabsorption and Enhanced Efficiency. *Nano Lett.* **2014**, *14* (7), 4097–4101.
- (52) Meinardi, F.; Colombo, A.; Velizhanin, K. A.; Simonutti, R.; Lorenzon, M.; Beverina, L.; Viswanatha, R.; Klimov, V.; Brovelli, S. Large-Area Luminescent Solar Concentrators Based on ‘Stokes-Shift-Engineered’ Nanocrystals in a Mass-Polymerized PMMA Matrix. *Nat. Photonics* **2014**, *8*, 392–399.
- (53) Meinardi, F.; McDaniel, H.; Carulli, F.; Colombo, A.; Velizhanin, K. A.; Makarov, N. S.; Simonutti, R.; Klimov, V. I.; Brovelli, S. Highly Efficient Large-Area Colourless Luminescent Solar Concentrators Using Heavy-Metal-Free Colloidal Quantum Dots. *Nat. Nanotechnol.* **2015**, *10*, 878–885.
- (54) Meinardi, F.; Akkerman, Q. A.; Bruni, F.; Park, S.; Mauri, M.; Dang, Z.; Manna, L.; Brovelli, S. Doped Halide Perovskite Nanocrystals for Reabsorption-Free Luminescent Solar Concentrators. *ACS Energy Lett.* **2017**, *2* (10), 2368–2377.
- (55) Liu, W.; Lin, Q.; Li, H.; Wu, K.; Robel, I.; Pietryga, J. M.; Klimov, V. I. Mn<sup>2+</sup>-Doped Lead Halide Perovskite Nanocrystals with Dual-Color Emission Controlled by Halide Content. *J. Am. Chem. Soc.* **2016**, *138* (45), 14954–14961.
- (56) Das Adhikari, S.; Guria, A. K.; Pradhan, N. Insights of Doping and the Photoluminescence Properties of Mn-Doped Perovskite Nanocrystals. *J. Phys. Chem. Lett.* **2019**, *10* (9), 2250–2257.
- (57) Guria, A. K.; Dutta, S. K.; Adhikari, S. Das; Pradhan, N. Doping Mn<sup>2+</sup> in Lead Halide Perovskite Nanocrystals: Successes and Challenges. *ACS Energy Lett.* **2017**, *2* (5), 1014–1021.
- (58) Huang, G.; Wang, C.; Xu, S.; Zong, S.; Lu, J.; Wang, Z.; Lu, C.; Cui, Y. Postsynthetic Doping of MnCl<sub>2</sub> Molecules into Preformed  $\text{CsPbBr}_3$  Perovskite Nanocrystals via a Halide Exchange-Driven Cation Exchange. *Adv. Mater.* **2017**, *29* (29), 1700095.
- (59) Mir, W. J.; Jagadeeswararao, M.; Das, S.; Nag, A. Colloidal Mn-Doped Cesium Lead Halide Perovskite Nanoplatelets. *ACS Energy Lett.* **2017**, *2* (3), 537–543.
- (60) Ji, S.; Yuan, X.; Cao, S.; Ji, W.; Zhang, H.; Wang, Y.; Li, H.; Zhao, J.; Zou, B. Near-Unity Red Mn<sup>2+</sup> Photoluminescence Quantum Yield of Doped  $\text{CsPbCl}_3$  Nanocrystals with Cd Incorporation. *J. Phys. Chem. Lett.* **2020**, *11* (6), 2142–2149.
- (61) Das Adhikari, S.; Behera, R. K.; Bera, S.; Pradhan, N. Presence of Metal Chloride for Minimizing the Halide Deficiency and Maximizing the Doping Efficiency in Mn(II)-Doped  $\text{CsPbCl}_3$  Nanocrystals. *J. Phys. Chem. Lett.* **2019**, *10* (7), 1530–1536.
- (62) Paul, S.; Bladt, E.; Richter, A. F.; Döblinger, M.; Tong, Y.; Huang, H.; Dey, A.; Bals, S.; Debnath, T.; Polavarapu, L.; Feldmann, J. Manganese-Doping-Induced Quantum Confinement within Host Perovskite Nanocrystals through Ruddlesden–Popper Defects. *Angew. Chem., Int. Ed.* **2020**, *59* (17), 6794–6799.
- (63) Krieg, F.; Ong, Q. K.; Burian, M.; Rainò, G.; Naumenko, D.; Amenitsch, H.; Süess, A.; Grotevent, M. J.; Krumeich, F.; Bodnarchuk, M. I.; Shorubalko, I.; Stellacci, F.; Kovalenko, M. V. Stable Ultraconcentrated and Ultradilute Colloids of  $\text{CsPbX}_3$  (X = Cl, Br) Nanocrystals Using Natural Lecithin as a Capping Ligand. *J. Am. Chem. Soc.* **2019**, *141* (50), 19839–19849.
- (64) Krieg, F.; Ochsenbein, S. T.; Yakunin, S.; ten Brinck, S.; Aellen, P.; Süess, A.; Clerc, B.; Guggisberg, D.; Nazarenko, O.; Shynkarenko, Y.; Kumar, S.; Shih, C.-J.; Infante, I.; Kovalenko, M. V. Colloidal  $\text{CsPbX}_3$  (X = Cl, Br, I) Nanocrystals 2.0: Zwitterionic Capping Ligands for Improved Durability and Stability. *ACS Energy Lett.* **2018**, *3* (3), 641–646.
- (65) Xu, K.; Meijerink, A. Tuning Exciton–Mn 2+ Energy Transfer in Mixed Halide Perovskite Nanocrystals. *Chem. Mater.* **2018**, *30* (15), 5346–5352.
- (66) De Siena, M. C.; Sommer, D. E.; Creutz, S. E.; Dunham, S. T.; Gamelin, D. R. Spinodal Decomposition During Anion Exchange in Colloidal Mn 2+ -Doped  $\text{CsPbX}_3$  (X = Cl, Br) Perovskite Nanocrystals. *Chem. Mater.* **2019**, *31* (18), 7711–7722.
- (67) Liu, H.; Wu, Z.; Shao, J.; Yao, D.; Gao, H.; Liu, Y.; Yu, W.; Zhang, H.; Yang, B.  $\text{CsPb}_{1-x}\text{Mn}_x\text{Cl}_3$  Perovskite Quantum Dots with High Mn Substitution Ratio. *ACS Nano* **2017**, *11* (2), 2239–2247.
- (68) Mahamuni, S.; Lad, A. D.; Patole, S. Photoluminescence Properties of Manganese-Doped Zinc Selenide Quantum Dots. *J. Phys. Chem. C* **2008**, *112* (7), 2271–2277.
- (69) Song, P.; Qiao, B.; Song, D.; Cao, J.; Shen, Z.; Xu, Z.; Zhao, S.; Wageh, S.; Al-Ghamdi, A. Modifying the Crystal Field of  $\text{CsPbCl}_3:\text{Mn}^{2+}$  Nanocrystals by Co-Doping to Enhance Its Red Emission by a Hundredfold. *ACS Appl. Mater. Interfaces* **2020**, *12* (27), 30711–30719.
- (70) Cottrell, T. L. *The Strengths of Chemical Bonds*, 2nd ed.; Butterworth: London, 1958.
- (71) Lehmann, E. H.; Vontobel, P.; Wiesel, L. Properties of the Radiography Facility NEUTRA at SINQ and Its Potential for Use as European Reference Facility. *Nondestr. Test. Eval.* **2001**, *16* (2–6), 191–202.
- (72) Morad, V.; McCall, K. M.; Sakhatskyi, K.; Lehmann, E.; Walfort, B.; Losko, A. S.; Trtik, P.; Strobl, M.; Yakunin, S.; Kovalenko, M. V. Luminescent Lead Halide Ionic Liquids for High-Spatial-Resolution Fast Neutron Imaging. *ACS Photonics* **2021**, DOI: 10.1021/acspophotonics.1c01348.